We are IntechOpen,
the world's leading publisher of
Open Access books
Built by scientists, for scientists

6,900
Open access books available

186,000
International authors and editors

200M
Downloads

Our authors are among the

154
Countries delivered to

TOP 1%
most cited scientists

12.2%
Contributors from top 500 universities

CLARIVATE ANALYTICS
BOOK CITATION INDEX
INDEXED

WEB OF SCIENCE™

Selection of our books indexed in the Book Citation Index
in Web of Science™ Core Collection (BKCI)

Interested in publishing with us?
Contact book.department@intechopen.com

On Performance of S-band FMCW Radar for Atmospheric Measurements

Turker Ince
Izmir University Of Economics
Turkey

1. Introduction

At low microwave frequencies, radars respond to spatial variations in the index of refraction of the air often characterized by the atmospheric refractive-index structure parameter, C_n^2. While remote measurement of the atmospheric boundary layer (ABL) is complicated by the low radar reflectivity of clear-air turbulence structures, frequency-modulated, continuous-wave (FMCW) radars, having tremendous sensitivity and spatial resolution compared to their pulsed counterparts, have proven to be a solution to this problem. While Doppler capability can be added to FMCW radars (Strauch et al., 1976), the unique strength of this technology lies in its ability to monitor the atmospheric refractive-index structure parameter, C_n^2, with unparalleled resolution in height and time. Since the first high-resolution atmospheric FMCW radar, developed by Richter (1969), a number of FMCW radars have been developed for high-resolution atmospheric probing (Chadwick et al., 1976; Eaton et al., 1995; Hirsch, 1996), which have provided valuable information about the fine structure and dynamics of clear-air turbulence. The advent of S-band, FMCW radars has opened a new research field, which was reviewed by Gossard (1990).

Microwave backscattering from the clear-air ABL is generally a combination of Bragg scattering from small-scale spatial variations in refractive index caused by turbulence and Rayleigh scattering from insects, birds, dust, or other airborne particles whose size is much smaller than the radar wavelength. At S-band frequencies, radars measure clear-air backscatter from both refractive index turbulence and from insects. Based on the experimental observations (Wilson et al., 1994; Eaton et al., 1995; Ince et al., 2003; Martin and Shapiro, 2007), Rayleigh scattering from insects can be the dominant source of clear-air returns in both the convective boundary layer (CBL) and the nocturnal boundary layer (NBL). Depending on an application, radar return from airborne insects may be considered either as source of clutter (such as contamination of weather radar measurements) or as desirable passive tracers of the clear air (Wilson et al., 1994). Due to its very fine spatial and temporal resolution, S-band FMCW radars are able to resolve individual insects and discriminate between discrete particle echoes and distributed clear-air echo.

Despite FMCW radars being excellent tools for turbulence studies in the convective ABL and in the capping inversion region (Eaton et al., 1995), relatively few atmospheric studies reported

in the literature have used FMCW radar data extensively for both quantitative and qualitative analysis of clear-air features observed. While S-band FMCW radars have been designed with the capability to obtain height and time resolutions of 1 m and 1 s, respectively, the degree to which these resolution limits are obtained in practice depends upon the properties of the atmospheric echo itself. Range measurement errors due to non-zero Doppler velocities and finite coherence of the clear-air echo have implications on both spatial resolution and Doppler estimation of FMCW radars. Although the theoretical background for FMCW radars is well established, their measurement limitations for atmospheric targets and performance impact for atmospheric applications has received limited attention in the literature.

The detailed review of the theory of operation of S-band FMCW radar and its application to atmospheric boundary layer profiling can be found in the literature (Eaton et al., 1995; Ince et al., 2003). In this study, performance aspects of atmospheric FMCW radars including the effects of range-Doppler ambiguity, parallax typical of two-antenna radar systems, and near-field operation are discussed. The data collected during recent field experiments by the high-resolution S-band FMCW radar, described in Ince et al. (2003), is used to illustrate system performance. Analysis of FMCW radar signatures of atmospheric targets detectable at S-band frequencies has been performed by extracting both qualitative morphological information and quantitative information on the intensity of backscattered power from clear-air turbulence.

2. Principles

Frequency-modulated, continuous-wave (FMCW) radars may be thought of as a limiting case of pulse-compression radar where the duty cycle of the transmitted waveform approaches 100%. They operate by transmitting a long, coded waveform of duration T and bandwidth B. The improvement factor they gain over pulsed radars of equivalent range resolution is given by the time-bandwidth product of the waveform BT, which is often referred to as the compression gain. In FMCW systems, this gain can be very large, exceeding 60 dB. While several types of frequency coding may be used to yield the bandwidth B, linear frequency modulation is the simplest and most commonly used method in atmospheric FMCW radars.

Consider an FMCW radar that transmits constant amplitude linear FM signal of the form

$$s(t) = \exp(jwt + j(a/2)t^2), \qquad \text{-}T/2 < t < T/2 \tag{1}$$

where w is the radian frequency and a is the chirp rate in rad/s^2. The echo from an atmospheric target is essentially a delayed, attenuated, and possibly Doppler-shifted replica of the transmitted signal. The echo is demodulated by mixing it with a portion of the transmitted signal and low-pass filtering the result. The resulting beat frequency for a point target at range R_0, moving at radial velocity u_r, is given by

$$f_r(t) = -\left(\frac{2u_r}{\lambda} + \frac{2R_0}{c}\dot{f} + \frac{4u_r}{c}\dot{f}t\right), \tag{2}$$

where λ is the electromagnetic wavelength and $\dot{f} = a/2\pi = B/T$ is the chirp rate in Hz/s. Here, the first term represents the Doppler frequency shift, f_D, due to radial motion, and the second term represents the shift due to the nominal range of the target, which is exploited primarily by the FMCW radar. The final term represents a defocusing due to the dilation of the reflected signal's bandwidth due to the dependence of Doppler frequency to carrier frequency. For lower atmospheric velocities, the effect of the last term on the bandwidth of the echo may be safely ignored. Thus, for the case of stationary radar and targets, the beat frequency is linearly proportional to range.

Signal processing of the echo usually involves matched filtering, which is most commonly implemented for all ranges simultaneously through spectral analysis via an FFT algorithm. In this case, the output of the matched filter, which gives the response of the linear FMCW radar to a moving point target, can be expressed as

$$y(R) = \frac{\sin\left[\pi\left(f_D T + (R - R_0)/\Delta R\right)\right]}{\pi\left(f_D T + (R - R_0)/\Delta R\right)}, \tag{3}$$

where f_D is the Doppler frequency, and $\Delta R = c/(2B)$ is the expected range resolution for a transmitted bandwidth $B = \dot{f}T$. It is worth noting that this result is equivalent to impulse response of linear FMCW radar.

For FMCW Doppler radar, Doppler information can be retrieved on a sweep-to-sweep basis by analyzing the sequence of echoes from a particular range, as discussed by Strauch et al. (1976). In this case, the sampling frequency is the reciprocal of the sweep period T, the Nyquist Doppler frequency is $1/2T$, and resulting in an unambiguous Doppler velocity interval of $|u_r| \leq \lambda/4T$ assuming that range measurement errors due to Doppler can be ignored. Conventionally, two-dimensional FFT is performed on received signals to obtain range and Doppler frequency (velocity) spectrum.

The received mean power of a bistatic weather radar from a distributed atmospheric target of uniform reflectivity η, for circularly symmetric Gaussian shape antenna patterns, is given by Doviak & Zrnic (1993),

$$\bar{P}(R) = \frac{P_t G_t G_r \lambda^2 \Theta_1^2 \Delta R}{(512 \ln 2)\pi^2 R^2}\eta, \tag{4}$$

where P_t is transmitted power, G_t and G_r are transmit and receive antenna gains, Θ_1 is the one-way 3 dB beamwidth, ΔR is range resolution, and λ is radar wavelength. To better estimate η from the measured echo power at the output of receiver, the radar system must be calibrated. Based on Tatarskii's theory of electromagnetic wave propagation in a turbulent atmosphere (Tatarskii, 1961) and Ottersten's work in his 1969 landmark paper (Ottersten, 1969), clear-air radars can measure the refractive-index structure parameter (C_n^2)

from radar backscattered power. For Bragg scattering from refractive index fluctuations due to homogeneous, isotropic turbulence, η is commonly related to C_n^2 by Ottersten' well-known equation:

$$\eta = 0.38 C_n^2 \lambda^{-1/3}.$$

(5)

This equation assumes that the Bragg wavenumber, $k_B = 4\pi/\lambda$ lies within the inertial subrange. Note that C_n^2 in (5) is defined as an ensemble average. In practice, such averaging is performed over space or time assuming ergodicity. Therefore, for S-band radars, Bragg scatter from clear air depends much less on the wavelength of the radar than that of Rayleigh scatter (λ^{-4} dependence) by airborne particles.

3. Performance Analysis

3.1 Range and Doppler
FMCW radar performance characteristics, such as range-Doppler coupling, can be seen from analysis of (3), which is also ambiguity function for linear FMCW signal. The presence of both range and Doppler terms in the argument of the sinc function illustrates the effect of target motion on the radar's ability to locate. Figure 1 shows a typical two-dimensional time delay (range) – Doppler (velocity) ambiguity surface for a linear FMCW signal with time-bandwidth product of 1000. As seen from Figure 1, maximum unambiguous Doppler can be increased (by decreasing sweep period) at the expense of range ambiguity, or alternatively increasing maximum range results in Doppler ambiguity. By rearranging the terms in the argument in (3), the apparent range of the target can be expressed as $R_{app} = R_0 - f_D T \Delta R$, where it is easy to see that range mislocation by one resolution cell occurs when $f_D T = 1$, or $u_r = \pm \lambda / 2T$ which also corresponds to the Nyquist velocity interval for FMCW Doppler radar. Therefore, targets with unambiguously measured velocities are misregistered by no more than one half a resolution cell, or misregistration occurs when target velocities are aliased.

Additionally, the coherence of the atmospheric target during the sweep interval will limit range resolution of linear FMCW radar. For complex moving targets and for volume scattering, the coherence time (or the reciprocal of the Doppler spectral width) of the echo will limit resolution. A distribution of Doppler velocities observed over an integration time, T, will yield a distribution of apparent ranges. The resulting rms spread in range is determined by the transformation of the Doppler spectrum to the range domain using the relationship $R_{app} = R_0 - f_D T \Delta R,$

$$\sigma_R = \sigma_f (T \Delta R),$$

(6)

where σ_f is the Doppler spectral width of the echo. From this relation, it is apparent range resolution and sensitivity are optimized by matching the sweep time to the reciprocal of the Doppler bandwidth of the echo. In this case, the range spreading is equal to the range resolution, and the entire Doppler spectrum is confined to one range bin. No improvement in sensitivity or in resolution is achieved by increasing sweep time beyond this value, as the resulting echo simply spreads to adjacent range bins.
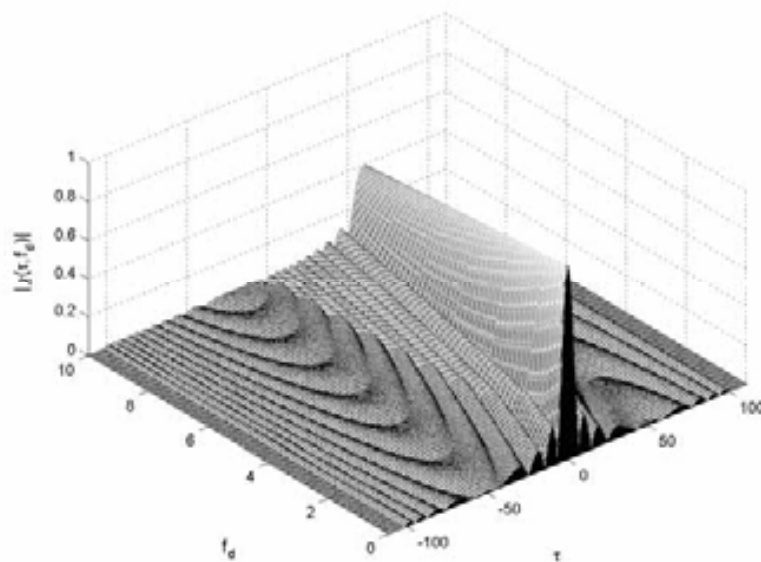
Fig. 1. The ambiguity surface for a linear FMCW signal with BT = 1000.

To maximize resolution and sensitivity, it is desirable to make both bandwidth and sweep time as large as possible. The effective value of sweep time is however constrained by the coherence time of the atmospheric echo. For example, a sampling volume with rms radial velocity of 1 m/s has a spectral width of 20 Hz at 3 GHz implying a coherence time of approximately 50 ms.

3.2 Parallax and Near-field Operation

From the weather radar equation (4), the received mean power can be correctly estimated only if radar targets are in the far field of antenna, that is $R > 2D^2/\lambda$, where D is the diameter of the antenna. Additionally, for bistatic FMCW radar employing two spatially separated antennas, a correction of the received power is necessary at near ranges to account for the reduced beam overlap. For Gaussian shaped beams aligned with their axes parallel, the antenna parallax function, or fractional beam overlap is given by Ince et al. (2003),

$$C_p(R) = \exp(-2\ln 2 \frac{d^2}{\Theta_1^2 R^2}),$$

(7)

where d is the separation distance between transmit and receive antennas, and Θ_1 is the one-way half-power beamwidth. Note that parallax results in an apparent reflectivity reduction and parallax error of backscattered power becomes significant within the radiating near-field of the antennas such that assumption of a far-field Gaussian beam pattern is not valid. It is also worth noting that the far-field criterion, $R_f = 2D^2 / \lambda$, is based on a conservative specification of maximum phase error, significant effects on the shape of the main lobe are not evident until $R \approx R_f / 4$ (Hansen, 1985).

FMCW atmospheric radars can measure boundary layer targets at minimum distances as close as 50 m. However, this minimum range lies in the Fresnel region in which antenna gain and pattern shape vary significantly with distance, and from (4) radar reflectivity is underestimated for targets in the near field. Based on the universal near-field reflectivity correction by Sekelsky (2002), 1 dB reduction in reflectivity at $R_f / 4$ is indicated, and at closer ranges ($R < R_f / 4$) near-field gain reduction becomes much more significant. Since at closer ranges the beam shape is no longer approximately Gaussian and is strongly dependent upon the particular antenna design, it is necessary to apply appropriate reflectivity correction for parallax and near-field gain reduction depending upon the parameters of radar system. In Figure 2, the relative importance of near field gain reduction and parallax for the parameters of the S-band FMCW radar system in Ince et al. (2003) is compared, and in this case parallax has the primary influence at close ranges.
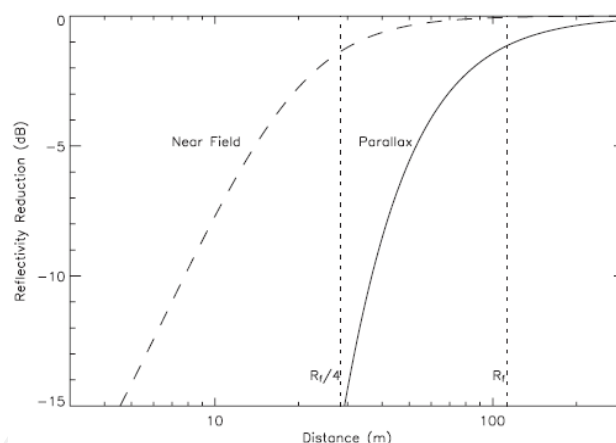

Fig. 2. Reflectivity reduction due to parallax (solid line) and near field (dashed line) effects for the parameters of the FMCW system in Ince et al. (2003).

4. Experimental Measurements

Data collected by the University of Massachusetts' high-resolution FMCW radar (Figure 3) during recent field experiments is used to illustrate system performance and analyze radar signatures of atmospheric targets detectable at S-band frequencies. Detailed description of this system and data processing can be found in Ince et al. (2003). The S-band FMCW radar system implements an internal calibration loop (by injecting into the receiver an attenuated and delayed sample of the high power amplifier output) to perform calibration of the atmospheric echo and estimate volume reflectivity.

Fig. 3. The University of Massachusetts S-Band FMCW radar system mounted on flatbed truck (electronics are contained within the cab).

Figure 4 shows one day continuous radar record of diurnal cycle of the ABL beginning at 14:27 local time (CDT, 19:27 UTC). The radar echo is expressed in terms of the logarithm of microwave C_n^2 obtained using (5), however, this representation is only meaningful for the clear-air component of the backscatter described by the Bragg scattering mechanism. In addition to distributed Bragg scatter from clear air, Figure 4 shows strong point echoes, which are in this study assumed to be entirely due to Rayleigh scatterers. It is worth noting that the distribution of Rayleigh scatter in reflectivity time-height image appears to reveal qualitatively additional boundary layer structure not otherwise detectable at S-band. However, the effect of much stronger Rayleigh echo (due to much stronger wavelength dependence, λ^{-4} as opposed to $\lambda^{-1/3}$ for Bragg scattering) on quantitative backscattered signal information is adverse. Interestingly, with high spatio-temporal resolution capability of FMCW radar, by reducing time averaging to below 1 s in Figure 4, it becomes possible to see undulations of O(10 m) in the radar echo as a consequence of Doppler-induced range measurement error due to the flapping of bird's wings. It is estimated that under clear sky conditions vertical velocities of atmospheric echoes in general will contribute misregistration of about one range bin at most.

From Figure 4, four-hour time period of convective ABL (between 14:30 to 18:30 local time) is extracted to perform quantitative analysis of FMCW radar reflectivity. In this case, the collocated radiosonde (operated by NCAR/ATD) measurements of temperature and humidity show typical characteristic of convective ABL bounded above by dry air. In the three panels of Figure 5 respectively reflectivity, Doppler (vertical) velocity, and the correlation coefficient of successive echoes for one-hour of convective ABL are shown. The latter two products are the result of the pulse-pair processing (Doviak & Zrnic, 1993) averaged over 20 pulses (~1 s averaging).
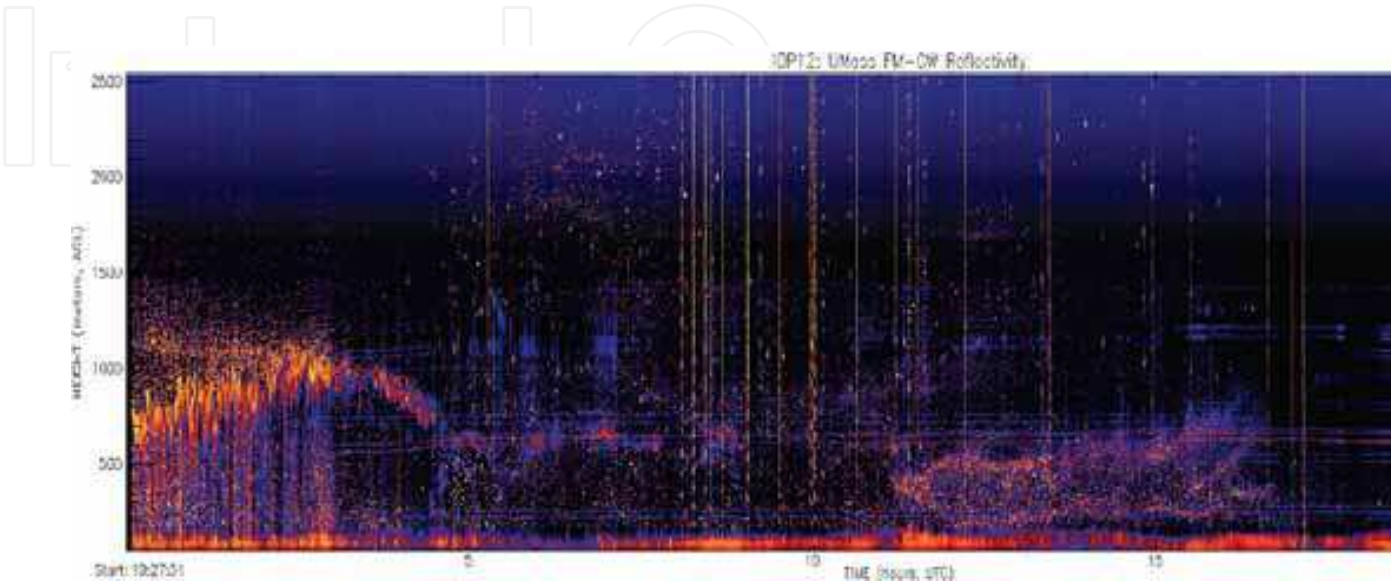
Fig. 4. S-band FMCW radar profiler image showing approximately 24-hour record of the ABL durin 26 Oct beginning at 14:27 CDT.
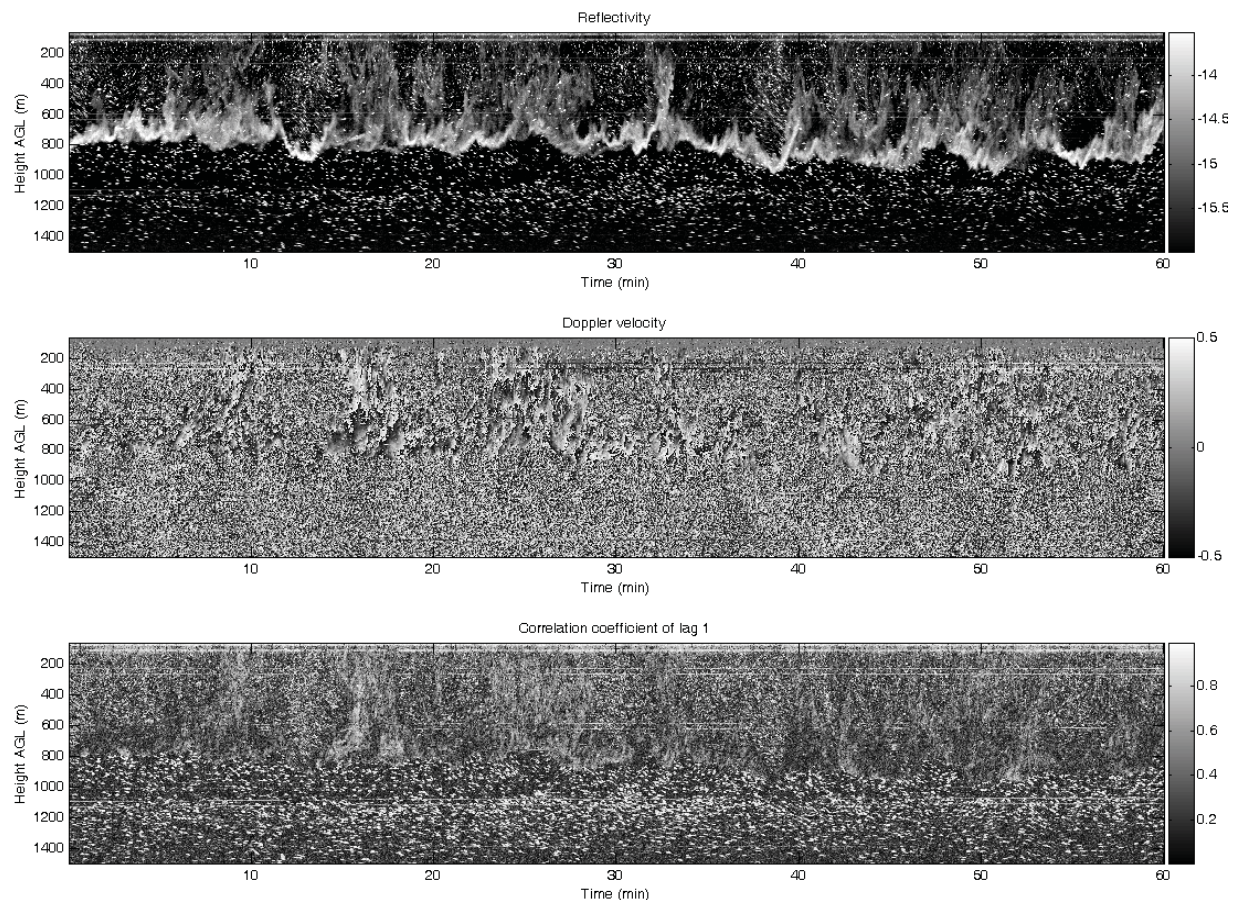
Fig. 5. First hour of convective ABL echo from Figure 4 showing reflectivity, Doppler velocity, and single-lag correlation coefficient.

The reflectivity image shows that initially significant Rayleigh backscatter is observed both above and below the capping inversion which peaks near 1000 m altitude at about 17:00 local time. After this time, both the Rayleigh scatter and the distributed Bragg scatter below the inversion decrease significantly, and the strong echo at the top of the boundary layer disappears. The velocity image which is derived from the phase of the single-lag covariance shows structure for some, but not all of the clear-air echo (due to velocity aliasing). The single-lag covariance panel shows extremely
high correlations for the Rayleigh scattering while the correlation coefficient for the Bragg scattering is relatively lower on average (due to larger spectral width of clear-air echo).
To discriminate the distributed clear-air echo from particulate scatter, a signal processing method based on the correlation coefficient of successive echoes can be applied to time-series of backscattered power. According to this method, magnitude of the sweep-to-sweep correlation coefficient is compared to an empirically determined threshold (in this case, a value of 0.8 is used) and high-correlation points (due to Rayleigh scatter) are removed and filled with estimated data by using least-squares interpolation (without affecting the statistics of the atmospheric clear-air echo). This processing allows estimation of atmospheric component of the clear air backscatter. Alternatively, median filtering can be applied to the two-dimensional radar reflectivity image to differentiate morphologically differing Bragg scatter (distributed echoes) and Rayleigh scatter (dot echoes). However, in

case of large density of particle echoes, their morphology will be similar to distributed scatter, hence the filter will not be able to separate two sources of scattering.
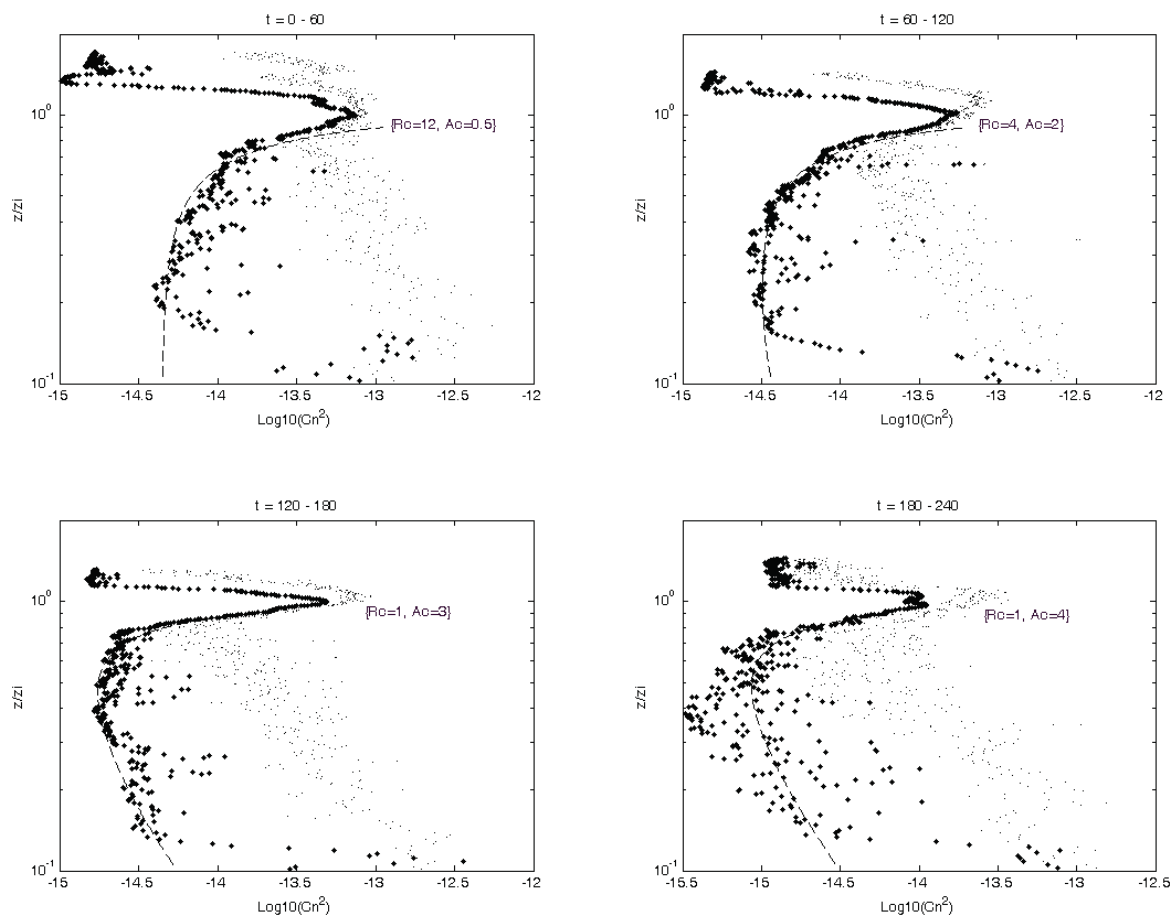
Fig. 6. Vertical profiles of estimated mean C_n^2 (large data points) obtained from post-processing over four consecutive 60-min periods. The small dotted profiles show the mean reflectivity including both Bragg and Rayleigh echo. The dashed lines are normalized profiles of C_n^2 based on the Fairall's model (1987).

In Figure 6, the computed vertical profiles of mean C_n^2 (estimated from postprocessed reflectivity) for four consecutive 60-min segments are plotted against height. The small dotted profiles show the corresponding mean reflectivity over the same intervals including both Bragg and Rayleigh echo. The star (*) profiles indicate estimated clear air component of the vertical profile over the 60-min interval. The vertical axis of each profile is scaled by the boundary layer depth, z_i, which can simply be obtained from the maximum of the reflectivity. Given the mean horizontal winds, the vertical profiles are roughly equivalent to a streamwise spatial average over approximately 10 km. Due to an increased number of insect echoes in the afternoon boundary layer and insect plumes (tracing sudden vertical motion from updrafts), Rayleigh scatterers dominate the observed profiles of mean reflectivity.

In this case, FMCW radar estimates of C_n^2 can be used to quantitatively test theoretical predictions on the ABL. In the free-convection boundary layer, C_n^2 is expected to follow a $z^{-4/3}$ power law, where z is height above ground level (Wyngaard & LeMone, 1980). From Figure 6, radar estimated C_n^2 increases with height inside convective mixed layer (between $0.2z_i$ and $0.9z_i$ the mean reflectivity follows a $z^{2/3}$ profile, a discrepancy of z^2) with an expected sharp turbulence induced peak at the top of the mixed layer ($\sim z_i$). Note in this case strong ground clutter affects C_n^2 measurements below $0.1z_i$. This observed discrepancy in C_n^2 from its mixed-layer prediction may be due to entrainment effects, which can be predicted by a model developed by Fairall (1987) based on a top-down and bottom-up diffusion approach in the entraining, convective boundary layer. In Figure 6, by choosing appropriate values for R_c and A_c parameters (respectively top-down and bottom-up components) of the model, the predicted normalized C_n^2 profiles is fitted to the vertical profiles of mean reflectivity from experimental data. Additionally, theoretical models on the shape of the reflectivity profile in the inversion region have been developed by Wyngaard & LeMone (1980). The existence of the reflectivity peak is known from in situ measurements (Wyngaard & LeMone, 1980) and from large-eddy simulation (Muschinski et al., 1999).

In Figure 7, log-variance of estimated C_n^2 over four consecutive 60-min periods is compared against the radiosonde-based potential temperature profiles. It can be seen that much higher variance occurs across the top of the convective boundary layer (corresponding to the height of the strongest potential temperature gradient) due to strong refractive index turbulence, and peak C_n^2 variance increases as the potential temperature jump across the inversion increases.
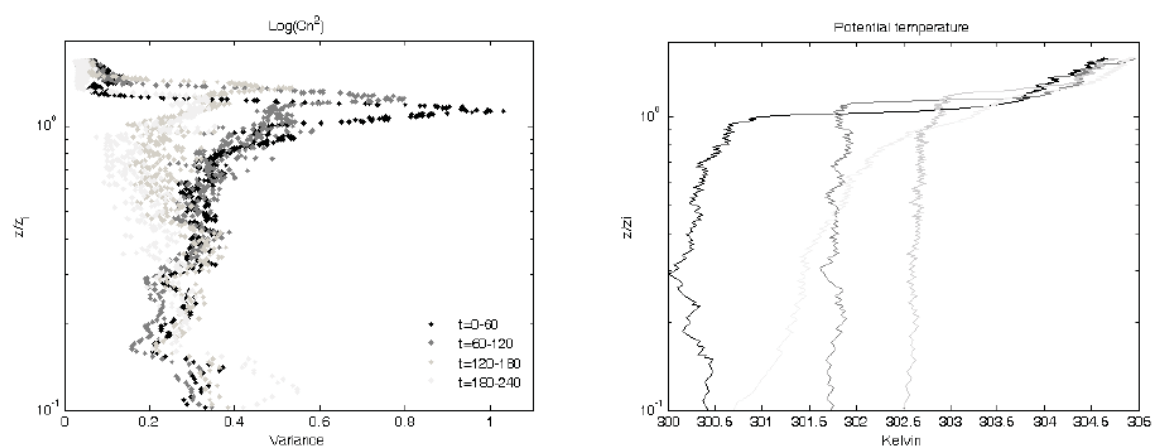

Fig. 7. The log-variance of estimated C_n^2 over four consecutive 60-min periods (left), and corresponding potential temperature profiles measured by radiosonde (right).

In Figure 8, radar reflectivity time-height image (starting at 0650 UTC in Figure 4) of nocturnal boundary layer turbulence below and insect layer within a low-level jet in the

NBL is shown. Collocated radiosonde profile of wind speed taken at 0658 UTC is shown in Figure 9. The FMCW reflectivity shows intensified turbulence and wave activity from surface extended to heights of about 150 m where sounding shows evidence of strong shear. Additionally, radiosonde wind measurements shows a low-level jet formed between heights 150 and 550 m with maximum winds of over 16 m/s at approximately 300 m height. In this case, a layer of insects detected by the radar at heights of the wind speed maximum helps reveal qualitatively this additional boundary layer structure.
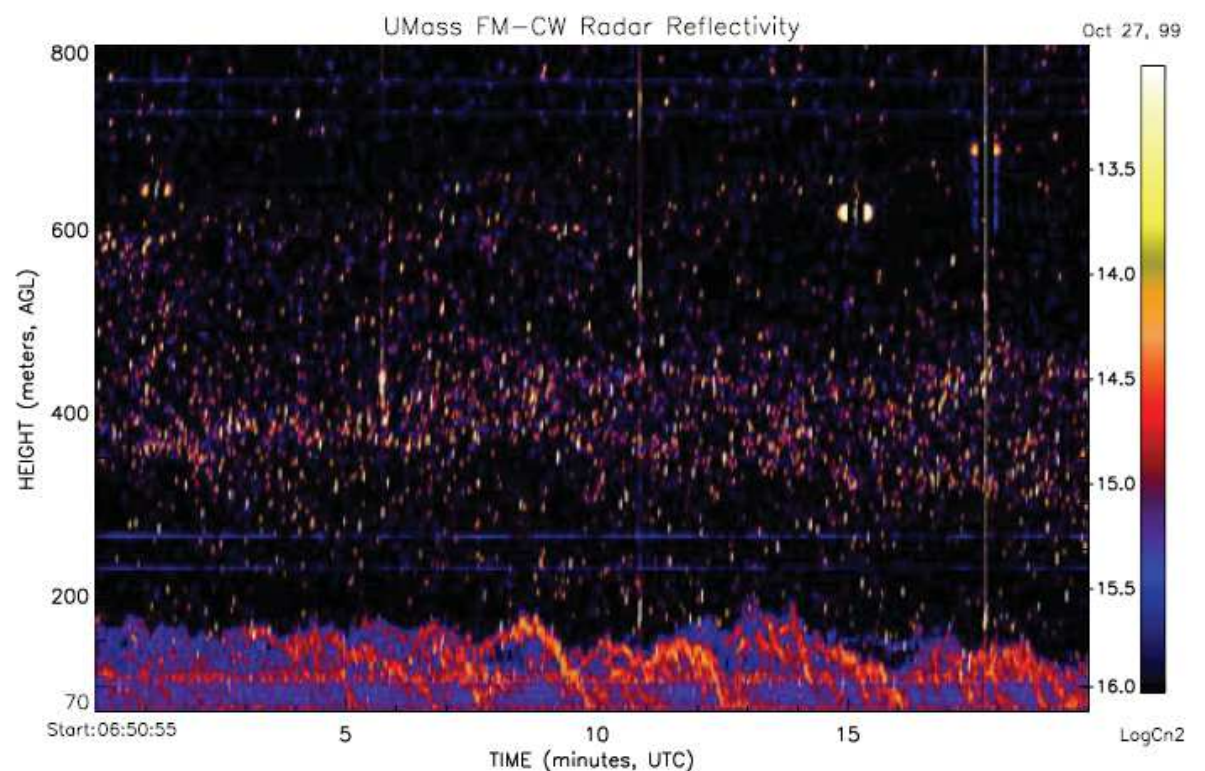
Fig. 8. Nocturnal boundary layer turbulence below and insects within a low-level jet observed at 0650 UTC.
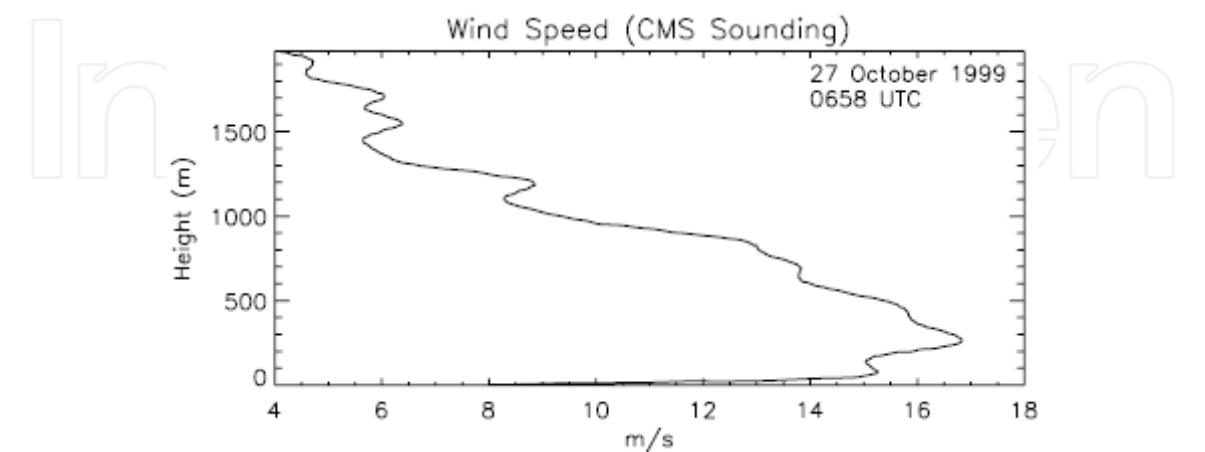
Fig. 9. Collocated radiosonde profile of wind speed at 0658 UTC.

5. Conclusion

In this study we have discussed and illustrated system performance of FMCW radar detection of atmospheric targets at S-band frequencies. In particular, the effects of non-zero Doppler velocities and finite coherence of the atmospheric echo on both spatial resolution of FMCW radars and on Doppler estimation have been presented. Additionally, we have considered parallax errors in reflectivity and near-field operation. For the clear-air atmosphere measurements, the S-band radar's sensitivity to Bragg and Rayleigh scattering and the effect of Rayleigh scatterers on vertical profiles of mean radar reflectivity have been illustrated. Experimental data collected by the high-resolution atmospheric FMCW radar has been used to perform analysis of S-band radar signatures of atmospheric targets and to quantitatively test theoretical predictions on the atmospheric boundary layer.

6. References

Chadwick, R.B.; Moran, K.P.; Strauch, R.G.; Morrison, G.E. & Campbell, W.C. (1976). Microwave radar wind measurements in the clear air. *Radio Science*, vol. 11, pp. 795–802.

Doviak, R.J. & Zrnic, D.S. (1993). *Doppler Radar and Weather Observations*. 2d ed. Academic Press, ISBN-10 : 0122214226.

Eaton, F.D.; McLaughlin, S.A. & Hines, J.R. (1995). A new frequency-modulated continuous wave radar for studying planetary boundary layer morphology. *Radio Science*, vol. 30, pp. 75–88.

Fairall, C. W. (1987). A top-down and bottom-up diffusion model of Ct2 and Cq2 in the entraining convective boundary layer. *J. Atmos. Sci.*, vol. 44, pp. 1009-1017.

Gossard, E.E. (1990). Radar research on the atmospheric boundary layer, In: *Radar in Meteorology*, edited by D. Atlas, pp. 477-527, Amer. Meteor. Soc., Boston.

Hansen, R. C. (1985). Aperture theory, In: *Microwave Scanning Antennas*, vol. 1, edited by R. C. Hansen, Penninsula, Los Altos, Calif.

Hirsch, L. (1996). Spaced-antenna-drift measurements of the horizontal wind speed using a FMCW-radar-RASS. *Contr. Atmos. Phys.*, vol. 69, pp. 113–117.

Ince, T. ; Frasier, S.J.; Muschinski, A. & Pazmany, A.L. (2003). An S-band frequency-modulated continuous-wave boundary layer profiler: Description and initial results. *Radio Science*, vol. 38, no. 4, pp. 1072–1084.

Martin, W.J. & Shapiro, A. (2007). Discrimination of bird and insect radar echoes in clear air using high-resolution radars. *J. Atmos. Oceanic Technol.*, vol. 24, pp. 1215–1230.

Muschinski, A.; Sullivan, P.P.; Wuertz, D.B.; Hill, R.J.; Cohn, S.A.; Lenschow, D.H. & Doviak, R.J. (1999). First synthesis of wind-profiler signals on the basis of large-eddy simulation data. *Radio Science*, vol. 34, pp. 1437-1459.

Ottersten, H. (1969). Atmospheric structure and radar backscattering in clear air. *Radio Science*, vol. 12, no. 4, pp. 1179–1193.

Richter, J. (1969). High-resolution tropospheric radar sounding. *Radio Science*, vol. 4, pp. 1261–1268.

Sekelsky, S. M. (2002). Near-field reflectivity and antenna boresight gain corrections for millimeter wave atmospheric radars. *J. Atmos. Oceanic Technol.*, vol. 19, pp. 468–477.

Strauch, R.G.; Campbell, W.C.; Chadwick, R.B. & Moran, K.P. (1976). Microwave FM-CW Doppler radar for boundary layer probing. *Geophys. Res. Lett.*, vol. 3, pp. 193–196.

Tatarskii, V. I. (1961). *Wave Propagation in a Turbulent Medium*. McGraw-Hill, New York.

Wilson, J.W.; Weckwerth, T.M.; Vivenkanandan, J.; Wakimoto, R.M. & Russell, R.W. (1994). Boundary layer clear-air radar echoes: Origin of echoes and accuracy of derived winds. *J. Atmos. Oceanic Technol.*, vol. 11, pp. 1184–1206.

Wyngaard, J.C. & LeMone, M.A. (1980). Behavior of the refractive index structure parameter in the entraining convective boundary layer. *J. Atmos. Sci.*, vol. 37, pp. 1573-1585.

.

Advances in Geoscience and Remote Sensing

Edited by Gary Jedlovec

Remote sensing is the acquisition of information of an object or phenomenon, by the use of either recording or real-time sensing device(s), that is not in physical or intimate contact with the object (such as by way of aircraft, spacecraft, satellite, buoy, or ship). In practice, remote sensing is the stand-off collection through the use of a variety of devices for gathering information on a given object or area. Human existence is dependent on our ability to understand, utilize, manage and maintain the environment we live in - Geoscience is the science that seeks to achieve these goals. This book is a collection of contributions from world-class scientists, engineers and educators engaged in the fields of geoscience and remote sensing.

How to reference

In order to correctly reference this scholarly work, feel free to copy and paste the following:

INTECH
open science | open minds